JACS
JOURNAL OF THE AMERICAN CHEMICAL SOCIETY

Article

pubs.acs.org/JACS

Morphology Evolution of High Efficiency Perovskite Solar Cells via Vapor Induced Intermediate Phases

Lijian Zuo,[†,‡] Shiqi Dong,[†] Nicholas De Marco,[†,‡] Yao-Tsung Hsieh,[†,‡] Sang-Hoon Bae,[†,‡] Pengyu Sun,[†] and Yang Yang*[,†,‡]

[†]Department of Materials Science and Engineering, University of California, Los Angeles, California 90095, United States
[‡]California NanoSystems Institute, University of California, Los Angeles, California 90095, United States

Supporting Information

ABSTRACT: Morphology is critical component to achieve high device performance hybrid perovskite solar cells. Here, we develop a vapor induced intermediate phase (VIP) strategy to manipulate the morphology of perovskite films. By exposing the perovskite precursor films to different saturated solvent vapor atmospheres, e.g., dimethylformamide and dimethylsufoxide, dramatic film morphological evolution occurs, associated with the formation of different intermediate phases. We observe that the crystallization kinetics is significantly altered due to the formation of these intermediate phases, yielding highly crystalline perovskite films with less defect states and high carrier lifetimes. The perovskite solar cells with the reconstructed films exhibits the highest power conversion efficiency (PCE) up to 19.2% under 1 sun AM 1.5G irradiance, which is among the highest planar heterojunction perovskite solar cells. Also, the perovskite solar cells with VIP processing shows less hysteresis behavior and a stabilized power output over 18%. Our work opens up a new direction for morphology control through intermediate phase formation, and paves the way toward further enhancing the device performances of perovskite solar cells.

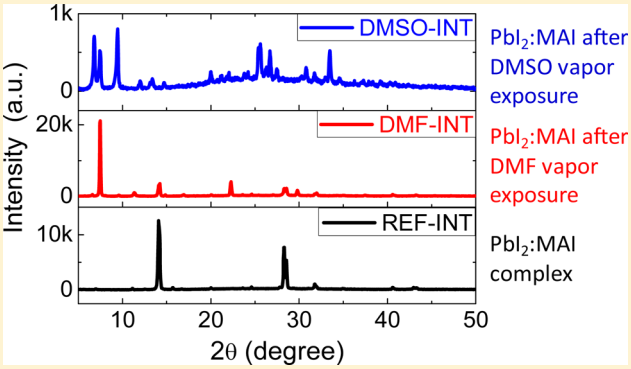

INTRODUCTION

Organic−inorganic halide perovskite based solar cells, e.g., $CH_3N_3HPbI_{3-x}Cl_x$, are recognized as one of the most promising candidates for future solar energy utilization, which have rapidly turned into the focus of intensive academic research and industrial interests in recent years.[1−4] The active layers of perovskite solar cells feature of mixed ionic−covalent bonding ABX_3 structures (A is cation, B is core metal, X is the anion),[5,6] which possess the advantages of a large dielectric constant,[7] high carrier mobility,[8] long carrier lifetime,[9,10] significantly shallow trap states,[11,12] and more. These merits have enabled perovskite solar cells to reach highest certified power conversion efficiencies (PCE) over 22%, which is comparable to that of commercial silicon photovoltaic (PV) devices. Moreover, the perovskite film can be easily formulated using the facile solution-based processes on the flexible texture,[13,14] which makes perovskite solar cells cost-effective and ideally compatible with the roll-to-roll processing.[15−17] These achievements have encouraged perovskite solar cells as a prevailing technique in the future photovoltaic market.[1,18] However, high device performance critically relies on the quality of the perovskite films,[19−21] e.g., high crystallinity and few defects. The perovskite film quality is intimately related to the film formation process, which needs to be strictly controlled for high device performance.[22]

It has been demonstrated that the organic−inorganic halide perovskite can be prepared through the self-assembly of the mixed precursors via annealing.[23,24] Thus far, the processing methods for the perovskite films mainly included the solution one-[25] or two-step(s) methods,[26,27] vacuum deposition,[28] and vapor-assisted processes.[29] Among these, the two-step solution processing has shown great potential to achieve highly crystalline and homogeneous films, and has been frequently employed as model system for further study.[30,31] The morphology control protocols developed in context of the above processing methods focus on controlling the kinetics or dynamics of crystallization, e.g., by controlling the solvation status of the precursors,[32] use of additives,[33] tailoring the precursors compositions,[4,34] surface induction,[15,30,35] etc. During the crystallization process, the formation of the intermediate phases has shown to be a critical step toward morphological manipulation.[25,36−40] During the transition from the precursors to the crystalline perovskite film, the intermediate phases form that can facilitate the film reconstruction and significantly influence the crystallization kinetics.[25,38] Moreover, reconstructed perovskite film have shown excellent optoelectronic properties and enabled highly efficient perovskite solar cells.[39,40] However, the current

Received: September 25, 2016
Published: November 15, 2016

DOI: 10.1021/jacs.6b09656
J. Am. Chem. Soc. 2016, 138, 15710−15716

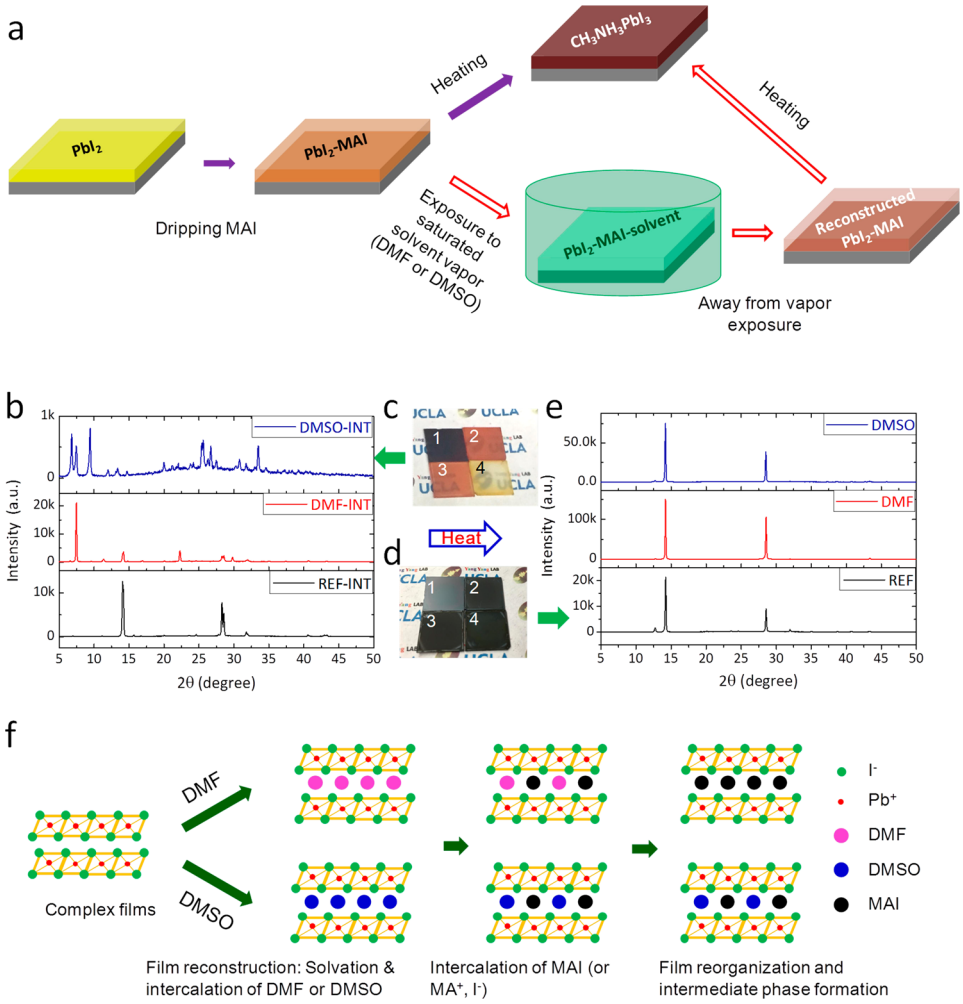

Figure 1. Vapor induced intermediate phase (VIP) strategy. (a) Schematic diagram the solvent-vapor induced intermediate phase strategy. (b) XRD pattern of intermediate phases with or without vapor treatment. Pictures of the (c) intermediate phases complex and (d) perovskite films (top) Sample 1. Without vapor treatment, 2. With 2 s DMF vapor treatment, 3. With 6 s vapor treatment, and 4. With 6 s DMSO vapor treatment). (e) XRD patterns of perovskite films processed from different vapor treatments. (f) Plausible morphology evolution mechanism with the VIP processing.

strategy to generate the intermediate phases has utilized the one-step solution processes using dimethyl sufoxide (DMSO) additives.[32] Thus, a broad application of intermediate phase strategies remains unexplored in terms of both processing methods and intermediate phase species. The formation of these intermediate phases originates from coordinated bonds between the precursors and the solvent molecules, which makes the perovskite or the PbI_2 films extremely sensitive to the surrounding vapor atmosphere.[41−46]

Here, we demonstrated the intermediate phase can also be induced by exposing the precursor films into the saturated solvent vapor atmosphere, e.g., dimethylformamide (DMF) or DMSO. Highly efficient planar heterojunction perovskite solar cells with delicately controlled morphology were achieved via the vapor induced intermediate phases (VIP) strategy. By exposing the mixed perovskite precursor films to different saturated solvent vapor atmospheres, such as DMF and DMSO, different intermediate phases formed, that were associated with strong apparent changes of the films colors and surface textures. Subsequently, highly crystalline perovskite films with large grain sizes, less trap states, and long carrier lifetime were obtained due to the reconstructed crystallization process. The corresponding perovskite solar cells with VIP processing (DMF vapor) exhibited the highest PCE up to 19.2% (reverse scan), with reduced hysteresis (18.1%, forward scan) and highest steady state output power over 18 mW/cm^2 under 1 sun, AM 1.5G irradiance. The improved device performance can be attributed to the reduced defects in the perovskite film as verified by photoluminescence (PL), and transient photovoltage/photocurrent decay (TPV/TPC) measurements.

RESULTS AND DISCUSSION

Vapor Induced Intermediate Phases. The proposed VIP method includes four steps as shown in Figure 1. First, spin-coating lead iodide (PbI_2) solution on substrates to form a uniform PbI_2 film. Second, the PbI_2 film was dripped with methylammonium iodide (MAI) solution to form a dark red PbI_2-MAI compound film. Third, the film was quickly exposed to a saturated solvent atmosphere for 2−6 s during the spin-coating to generate an intermediate complex film. Finally, the complex film was annealed at 135 °C for 15 min in ambient air (relative humidity 40% at 25 °C) to produce a poly crystalline perovskite film. Compared to the traditional two-step processing (without step 3), dramatic changes of the film were observed with the VIP processing. Typically, the PbI_2 films showed a light yellow color after annealling, and change to

DOI: 10.1021/jacs.6b09656
J. Am. Chem. Soc. 2016, 138, 15710−15716

dark red (Figure 1c) with the dripping of MAI due to the formation of the perovskite structure. With the vapor treatments, the dark red color of the precursor films initially faded and became more transparent, followed by turning to a white-to-red hazy color (with DMF vapor, top inset of Figure 1) or white-to-yellow haze (Figure 1 c).

Figure 1b depicts the XRD patterns of the PbI_2-MAI complex films. As shown, the films without vapor treatment showed peaks at 14.1° and 28.6°, corresponding to the ⟨110⟩ and ⟨220⟩ faces of perovskite crystals as illustrated in previous works.[22] The appearance of perovskite peaks suggested that the precursors were directly converted into the perovskite structures upon MAI dripping in the traditional solution two-step method. However, a new peak at 28.3° appeared in the precursor films, and disappeared after converting into perovskite films with annealing on hot plate (Figure S1). The appearance of the peak at 28.3° might result from the incomplete conversion of the precursors into the perovskite structure after MAI dripping. However, with the VIP process, the XRD peaks corresponding to the perovskite structure disappeared. Instead, three peaks at low diffraction angles of 6.8°, 7.5° and 9.5° emerged with DMSO vapor treatment, and these peaks were attributed to the formation of PbI_2-MAI-DMSO complex as observed in previous work with one-step solution process.[36,39] Interestingly, with the DMF vapor treatment, a new and distinctly strong peak at 7.5° appeared, corresponding to a lattice spacing of ∼1.17 nm. These results clearly show that the solvent vapor treatment is an effective method to induce the formation of different intermediate phases. It is worth noting that the intermediate phases obtained by VIP processing with DMF vapor is unprecedented in literature. Thus, our work opens up a novel mechanism to converting the precursor films into perovskite.

To provide an insight into the intermediate phases structures, we further analyzed the composition of the intermediate phases via Fourier transform infrared spectroscopy (FTIR), as shown in Figure S2. Compared to those without any vapor treatment, the precursor complex films with DMSO treatment showed an apparent absorption peak at 1017 cm^{-1}, which can be attributed to the S═O vibration. This observation is consistent with the previous literature report, and confirms the existence of DMSO in the intermediate phases.[36] However, the FTIR spectra of PbI_2-MAI precursor complex films with DMF treatment were similar to those without vapor exposure, and no peaks corresponding to the DMF molecules were observed in perovskite films with the DMF vapor exposure. This implies that the intermediate phases with DMF exposure are free of DMF solvent molecules. Furthermore, we studied the XRD patterns of pure PbI_2 films with and without DMF or DMSO vapor treatment (Figure S3) and compared them with those of the PbI_2-MAI intermediate phases. The XRD pattern of pure PbI_2 showed strong diffraction peak at 12.7°. Additional diffraction peaks appeared at 9.5° and 9.0° with DMF vapor treatment, and at 9.9° and 9.4° with the DMSO vapor treatment. It is clear that the peaks positions of pristine PbI_2 after DMSO or DMF vapor exposure were significant different from that of intermediate phases of the PbI_2-MAI complexes. This implied the involvement of both MAI and PbI_2 component in the intermediate phases. Therefore, it is concluded that the intermediate phases are composed of PbI_2-MAI with DMF vapor treatment, and PbI_2-MAI-DMSO with the DMSO vapor treatment.

On the basis of the above analysis, plausible phase transition mechanisms from the vapor treatments are drawn in Figure 1d. First, the DMF or DMSO solvent molecules may facilitate the interdiffusion between the PbI_2 and MAI layers due to the solvation of the PbI_2-MAI complex film by the saturated DMF or DMSO vapor surroundings. Second, the DMF or DMSO vapor treatment assists the intercalation of the MAI molecule into the PbI_2 crystal lattice. It has been shown that the PbI_2 crystal exhibits lamellar structure with a plane of Pb^{2+} ions sandwiched between adjacent layers of hexagonally arranged iodide ions. The large interlayer space and weak interlayer interaction allow the intercalation of different guest molecules, resulting in the expansion of the interlayer distance along the *c* axis.[47] Due to the strong interaction between the PbI_2 and the DMF or DMSO molecules, the interlayer distance of PbI_2 is expanded by DMF or DMSO vapor treatment, as proved by the appearance of low diffraction angle peaks of PbI_2 films (Figure S3). Thereafter, the MAI molecules can be easily embedded into the lattice structure of PbI_2, which accounts for the origin of intermediate phase formation. Afterward, the DMF solvent molecule can escape from the intermediate phase due to the low boiling point and weak interaction with Pb^{2+}, resting the intercalated MAI component in the PbI_2 crystal lattice. In the case of DMSO exposure, the DMSO molecules remain in the intermediate phase due to their high boiling point and the stronger coordinated interaction with the Pb^{2+}. Interdiffusion between the PbI_2 and MAI is the most important step for the solution-processed two-step method, and we can see that the formation of intermediate phase can significantly influence the crystallization kinetics. As a result, changes in the morphologies of the perovskite films are expected with the solvent vapor treatment on PbI_2-MAI complex films, which were examined as follow.

Morphology of Perovskite Films. After annealing, most of the precursors complex films were converted into the perovskite polycrystalline film (Figure 1d) with distinct perovskite peaks at 14.1° and 28.6° (Figure 1c).[28] Interestingly, we observed that the precursor films with vapor exposure showed faster conversion into perovskite on hot plate. We found that the peak intensities of the perovskite films show large differences, and increased in the sequence of the traditional two-step process, DMSO and DMF vapor treatment. The stronger XRD peaks indicate the improvement in crystallinity with the DMSO or DMF vapor treatment. Besides, the perovskite film with vapor exposure showed weaker PbI_2 peak at 12.7°, indicating less content of PbI_2 component and more complete conversion with the intermediate phases.

Figure 2 shows the corresponding morphologies of perovskite films processed with or without the VIP processing. The perovskite films processed from the traditional two-step method showed grain size around 300 nm (Figure 2a and d). However, with DMF and DMSO vapor exposure, the grain size was enlarged to 500 and 450 nm, respectively, and the surface roughness also significantly increased. Altough the perovskite film with VIP strategy show textured surface, the whole film remain fully covered on the SnO_2 surface without any pinholes, which should not adversely influence the device performance. Also, the crystal size of the perovskite films with VIP processing increased as verified by the XRD pattern (Figure S4), where the ⟨110⟩ full-width-half-maximum of perovskite with DMF vapor annealing was significantly narrowed (0.10°) compared with that without vapor annealing (0.14°), corresponding to the crystal size of 84 and 60 nm according to the Scherrer's

DOI: 10.1021/jacs.6b09656
J. Am. Chem. Soc. 2016, 138, 15710−15716

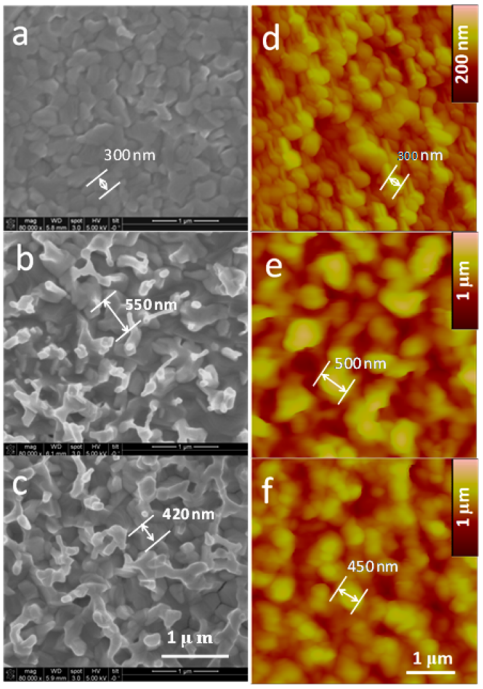

Figure 2. Morphology of the perovskite films. SEM and AFM images of perovskite film (a) and (d) processed from the traditional two-step process, (b) and (e) processed via DMF vapor treatment, (c) and (f) processed via DMSO treatment.

equation ($\tau = K\lambda/\beta \cos\theta$, where K is geometry factor, λ is the wavelength of X-ray, β is the half-peak width, and θ is the diffraction angle). Although the perovskite grain size became significantly larger, these large crystals were compactly arranged on the surface of ITO/SnO_2 substrates without any pin-holes, as confirmed by the cross-sectional images (Figure S5). The enlarged crystal size and more complete conversion from the precursor to the perovskite films verifies the vapor induced intermediate phases as an effective strategy to achieve high quality perovskite film.

Device Performance of Perovskite Solar Cells. The perovskite solar cell devices were fabricated using the perovskite films processed with different solvent vapor exposure. The conventional N–I–P device structure was adopted for device fabrication, which is shown in the Figure 3a. In this architecture, the SnO_2[48] and 2,2′,7,7′-Tetrakis(*N*,*N*-di-*p*-methoxyphenylamine)-9,9′-spirobifluorene (Spiro-OMeTAD)[49] were used as electron and hole conductors at ITO and Au electrodes, respectively. Figure 3b portrays the cross-sectional SEM image of the whole device. Figure 3c shows the *I*–*V* characteristics of the device, and the corresponding device parameters are summarized in Table 1. The control device

Table 1. Device Parameters of Perovskite Solar Cells with Different Vapor Treatments and Different Scan Direction

processing	scan direction	J_{SC} (mA/cm^2)	V_{OC} (V)	FF	PCE[a] (%)
REF	reverse	22.05	1.10	0.726	17.34 (16.25 ± 0.62)
REF	forward	21.73	1.04	0.693	15.52 (14.29 ± 0.53)
DMF	reverse	22.03	1.10	0.785	19.20 (17.92 ± 0.72)
DMF	forward	21.82	1.08	0.759	18.05 (16.75 ± 0.68)
DMSO	reverse	21.82	1.10	0.759	18.23 (16.75 ± 0.82)

[a]The device efficiency in the parentheses is the average value and standard deviation.

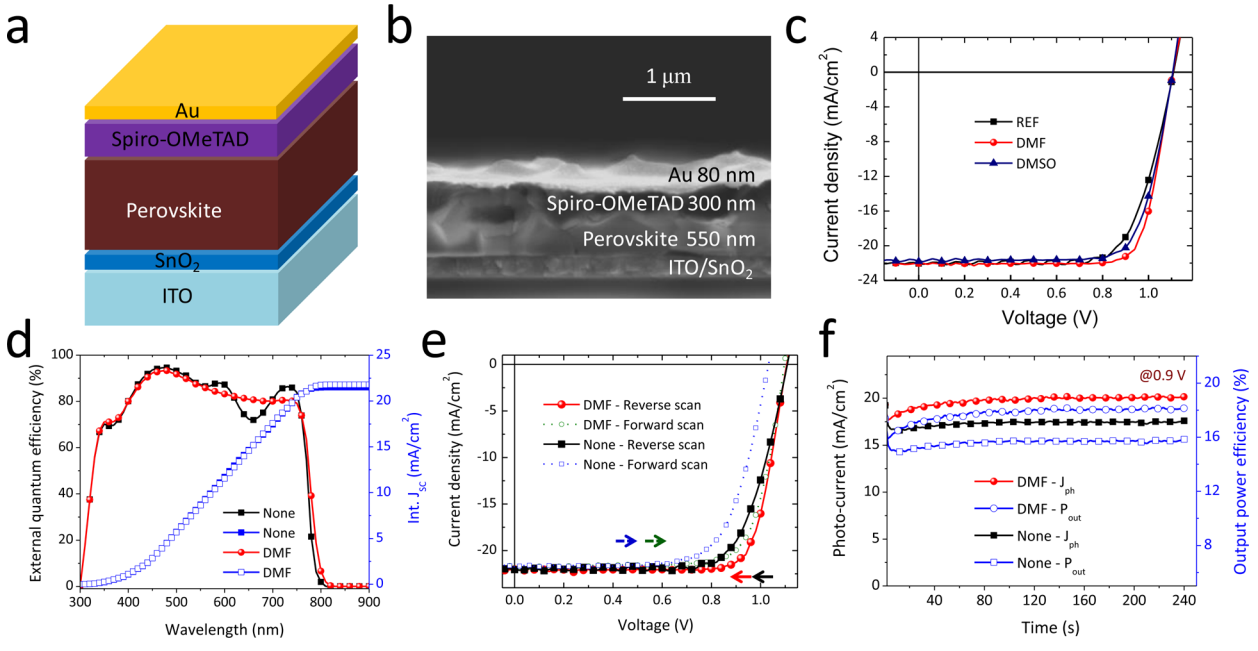

Figure 3. Device structure and performance of perovskite solar cells with or without VIP processing. (a) Device configuration of planar heterojunction perovskite solar cells. (b) Cross-section image of the perovskite solar cells. (c) *I*–*V* characteristic of perovskite solar cells with or without DMF, DMSO vapor treatment. (d) EQE spectra of perovskite solar cells with or without DMF vapor treatment. (e) Hysteresis *I*–*V* curves of perovskite solar cells with or without DMF vapor treatment. (f) Steady state output of perovskite solar cells with or without DMF vapor treatment (at 0.9 V bias).

DOI: 10.1021/jacs.6b09656
J. Am. Chem. Soc. 2016, 138, 15710–15716

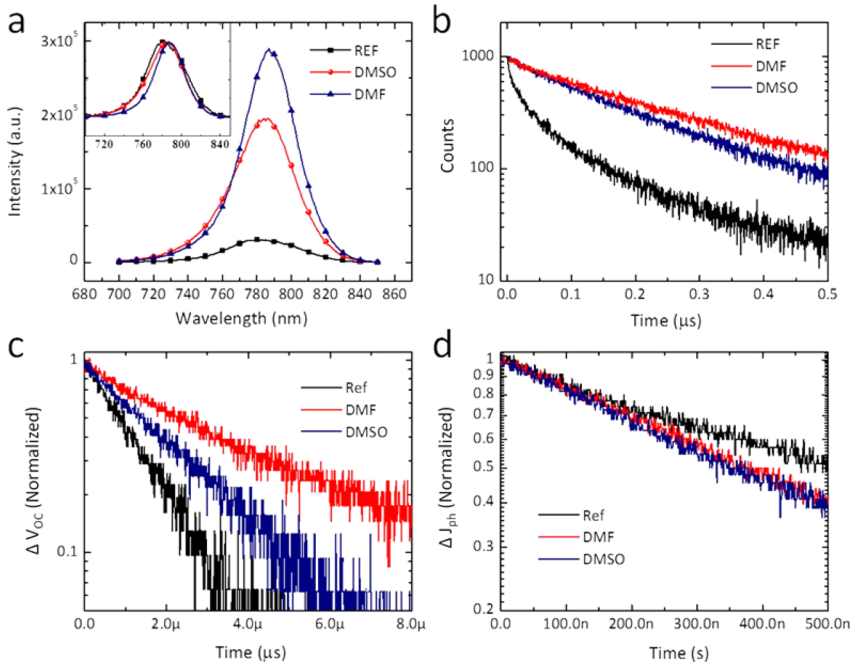

Figure 4. Carrier dynamics in perovskite films and perovskite solar cells. (a) Steady state PL spectra and (b) transient PL of perovskite film processed from different solvent vapors (None, DMF, and DMSO). (c) Transient photovoltage and (d) transient photocurrent of perovskite solar cells processed with different solvent vapor treatments (None, DMF, and DMSO).

processed with the traditional two-step method exhibited a best PCE of 17.34%, with V_{OC} of 1.10 V, J_{SC} of 22.05 mA/cm^2, and FF of 0.726. After the DMSO solvent vapor exposure, the device performance appreciably improved to 18.23%, with V_{OC} of 1.10 V, J_{SC} of 21.82 mA/cm^2, and FF of 0.759. With the DMF vapor treatment, the device performance was further enhanced to 19.20%, with V_{OC} of 1.10 V, J_{SC} of 22.03 mA/cm^2, and FF of 0.785, which stand among the highest in perovskite solar cells with planar heterojunction configuration. Variation in the device performances of perovskite solar cells from different batches were observed, and the statistic histogram for the device performance variation is shown in Figure S6. We also studied the effect of vapor treatment time on the device performance. As shown in Figure S7, the device performance of perovskite solar cells with a vapor treatment time from 2 to 6 s showed improvement, but dropped when exposure time is longer than 6 s due to the poor morphology. Figure 3d showed the external quantum efficiency of the perovskite solar cell with or without DMF vapor annealing. The highest EQE peak can reach up to 94%, implying the efficacy of the device configuration for light trapping and charge generation. The integrated J_{SC} from the EQE spectra of the perovskite solar cells without vapor annealing was as high as 21.44 mA/cm^2, and further improved to 21.66 mA/cm^2 with DMF vapor treatment. These values were consistent (less than 3% deviation) with the measured J_{SC} from the scanned $I-V$ curves, thus confirming the validity of the device performance. Although the integrated J_{SC}s of perovskite solar cells with or without vapor annealing were similar, the EQE spectra showed large differences. The EQE profiles of perovskite solar cells from DMF vapor treatment were more similar to the absorption spectra of the perovskite films (Figure S8), and the interference-induced peaks and valleys (EQE spectra of perovskite solar cells without vapor exposure, and Figure S9 for the simulated optical field distribution in the control device) disappeared. We simulated the EQE spectra of the perovskite solar cells to confirmed the origin of "V" shape, and ascribe it the a comprehensive effect of each layer via optical interference. As can be seen, the position of the "V" shape can be altered by changing the perovskite and spiro-OMeTAD layer thickness. Thereafter, the diminish of "V" shape EQE can be attributed to the increased surface roughness with DMF vapor treatment. The irregular light scattering of the rough perovskite layer can weaken the interference effect from the flat interface. This results indicates great potential of the VIP processing technique for optical manipulation in perovskite solar cells.

Hysteresis is typically observed in perovskite solar cells due to the defect states or surface charging induced by ion migration,[50] which can be related to a variety of factors, such as interfacial contact and morphology. Figure 3e shows the hysteresis effect of the $I-V$ curves for devices with the traditional two-step method and the DMF VIP processing. For the control device, a large discrepancy between the reverse and forward scan is observed, and the forward scan displays a lower FF (0.693), V_{OC} (1.04 V), and the overall PCE (15.52%), which represents over 10% reduction than that of the reverse scan (17.34%). For the devices with DMF vapor exposure, the device parameters for the forward scanned show a FF of 0.759, V_{OC} of 1.08 V, and overall PCE of 18.05%, which is within 6% deviation from that with reverse scan (19.20%). Thus, hysteresis can be appreciably suppressed by treating the film with DMF vapor. We attributed the alleviated hysteresis issue to the improved perovskite film quality, as described previously.

The appearance of $I-V$ hysteresis makes it difficult to judiciously evaluate true device performance from the $I-V$ curve scan. Thus, we further measured the steady state output at the maximum power point to justify device performance improvement from VIP processing. As shown in Figure 3f, the perovskite solar cells without solvent vapor treatment exhibits a maximum photocurrent of 17.5 mA/cm^2 at a bias of 0.90 V under 1 sun AM 1.5 G solar spectra, corresponding to the maximum power output of 15.75 mW/cm^2. With DMF vapor

DOI: 10.1021/jacs.6b09656
J. Am. Chem. Soc. 2016, 138, 15710−15716

exposure, the device showed a maximum power output of 18.09 mW/cm^2 (highest value), with the photocurrent of 20.1 mA/cm^2 at a 0.90 V bias. Both of the device show stable steady state output during 240 s (Figure S10). The stability of perovskite solar cells in ambient condition is recorded and shown in Figure S10. The perovskite solar cells show degradation over time, which can be ascribed to the moisture induced crystal collapse of perovskite film. And the device performance of perovskite solar cell with DMF VIP processing show imporved shelf stability possibly due to the improved crystallinity. This confirms the VIP technique as an efficient strategy to improve the device performance of perovskite solar cells.

Photo Carrier Dynamics. The improvement in the overall device performance with VIP originates from the FF, which is intimately related to the degree of traps or defect states in the perovskite films. We further examined the photo carrier dynamics in perovskite films by means of PL spectroscopy,[9,10,51] which has proven a useful tool to characterize carrier dynamics. It has been reported that the PL behavior of perovskite film is closely correlated with film morphology,[20] and that significant PL quenching can be induced by the defect states in the perovskite films.[51] Figure 4 shows the steady state PL spectroscopy of perovskite films on ITO/SnO_2 substrates with or without solvent vapor exposure. The excitation wavelength in this measurement is 640 nm, and emission spectra ranges from 700 to 850 nm, which covers the band edges of the $CH_3NH_3PbI_{3-x}Cl_x$. As can be seen, the PL intensity with DMF or DMSO vapor treatment shows significant enhancement by ∼600% and ∼900% compared to the film without any treatment. The PL intensity enhancement of perovskite films with DMF or DMSO vapor treatment implies the suppression of nonradiative charge recombination by the trap states in the bulk perovskite film. Besides the enhanced PL intensity, the PL spectra of perovskite films is slightly narrowed and PL peaks red-shifted with DMSO or DMF vapor treatment (inset of Figure 4a). This indicates a narrower distribution in the density of states or trap states due to the improved crystallinity. In the meanwhile, we measured the transient PL response of the perovskite films with or without the solvent vapor exposure. Different from the steady state PL spectra, the PL transient behavior provides a direct observation of different mechanisms of photocarrier annihilation. As shown, the PL of the perovksite films processed from the traditional two-step without VIP processing exhibited obvious biexponential decay, indicating two different channels for PL quenching. By fitting with both fast and long decay components, we derived two PL lifetimes with τ_1 of 17 ns, and τ_2 of 150 ns. Typically, the shorter lifetime can be attributed to filling of the trap states,[34] and longer lifetime originates from free carrier recombination.[34,52] With the solvent vapor exposure, the transient PL becomes a monoexponential in decay, and the short lifetime PL quenching channel disappeared. The suppression of short lifetime PL species implies that PL quenching via traps or defect states was suppressed with VIP technique, and verifies the reduction of defect states in the perovskite film. Furthermore, the carrier lifetime extended to 200 ns with DMF vapor treatment, and 160 ns with DMSO vapor treatment. These results demonstrate the effectiveness of the VIP strategy for constructing high quality perovskite films with reduced defects states.

During the operation of a real device photogenerated carriers, either free or excitonic, are largely separated at the interfaces of Spiro-OMeTAD/perovksite, resulting in strong PL annihilation by charge transfer at the interfaces. The separated charges can either recombine via surface trap states or be swept out of the device for electrical power generation. In this scenario, the techniques of transient photovoltage (TPV) and transient photocurrent (TPC) decay clearly show the photo carriers dynamics during the device operation. The decay of TPV traces the fates of carriers after separating at the electrode interfaces, which is observed to extract information regarding carrier lifetime within the whole device. The carrier lifetimes were taken as the time for which the photovoltage decayed to 1/e of its peak intensity. As portrayed in Figure 4c, the perovskite solar cells without VIP processing showed carrier lifetimes of 1.75 μs, whereas, the perovskite solar cell with DMF or DMSO treatment show significantly higher carrier lifetimes up to 4.2 and 2.3 μs, respectively. The elongated carrier lifetimes after charge transfer confirm the suppression of trap states in the bulk and at the interfaces. Furthermore, we monitored the transient behaviors of the photocurrent at short-circuit condition, where the carrier lifetime at short circuit condition indicates the carrier transit time from the perovskite films to the electrodes. Figure 4d shows the TPC curves of perovskite solar cells processed from different VIP processing. The devices without vapor treating showed lifetime of ∼700 ns, and shorten to ∼550 ns with both DMF and DMSO vapor treating. A possible reason for the slightly shortened lifetime with DMSO or DMF vapor treating is the increased carrier mobility of the perovskite films as induced by the improved crystallinity. The observations from the TPV and TPC were consistent with the device performance, and verify the efficacy of the VIP strategy for achieving high device performance in perovskite solar cells.

■ CONCLUSIONS

In summary, we demonstrated that the vapor induced intermediate phases (VIP) strategy is an effective method to control the morphology for highly efficient perovskite solar cells. VIP processing can facilitate the interdiffusion between the PbI_2 and MAI, thus enabling the formation of different intermediate phases as a transition from the precursor film into the perovskite polycrystalline films. The reconstructed perovskite films show larger crystal sizes and a reduced density of trap states. Consequentially, the perovskite solar cell efficiency is improved from 17.3% to 19.2%, which stands among the highest for planar heterojunction perovskite solar cells.

■ ASSOCIATED CONTENT

Supporting Information

The Supporting Information is available free of charge on the ACS Publications website at DOI: 10.1021/jacs.6b09656.

Experimental sections; XRD data of perovskite and perovskite precursor films; FTIR patterns of the intermediate phases; XRD patterns of PbI2 films with different vapor treating; Full half peak width of perovskite films processed with or without DMF vapor treating; SEM images of perovskite films and cross sectional images of perovskite solar cells; Histogram of perovskite solar cells efficiency variation; $I-V$ characteristic curves of perovskite solar cells with different vapor exposure time; Absorption and transmittance spectra of perovskite films with or without DMF vapor exposure; Optical field distribution in perovskite device; Device stability measurement (PDF)

DOI: 10.1021/jacs.6b09656
J. Am. Chem. Soc. 2016, 138, 15710−15716

AUTHOR INFORMATION

Corresponding Author

*yangy@ucla.edu

ORCID

Yang Yang: 0000-0001-8833-7641

Notes

The authors declare no competing financial interest.

ACKNOWLEDGMENTS

This work was financially supported by a grant from the Office of Naval Research (Grant No. N000141110250), UCLA Internal Funds, the UC-Solar Program (Fund Number MRPI 328368), and the Enli Tech (in Taiwan) for donating the EQE measurement system to UCLA. We also like to acknowledge Mr. Ryan Henry and Prof. Bruce Dunn for helping with the FTIR measurement. We thank Dr. Yajie Jiang, and Prof. Anito Ho-Baillie for providing the n and k values of the layers in perovskite devices.

REFERENCES

(1) Park, N.-G. *Mater. Today* **2015**, *18*, 65.
(2) Hodes, G. *Science* **2013**, *342*, 317.
(3) Stranks, S. D.; Snaith, H. J. *Nat. Nanotechnol.* **2015**, *10*, 391.
(4) Jeon, N. J.; Noh, J. H.; Yang, W. S.; Kim, Y. C.; Ryu, S.; Seo, J.; Seok, S. I. *Nature* **2015**, *517*, 476.
(5) Jung, H. S.; Park, N.-G. *Small* **2015**, *11*, 10.
(6) Chen, Q.; De Marco, N.; Yang, Y.; Song, T.-B.; Chen, C.-C.; Zhao, H.; Hong, Z.; Zhou, H.; Yang, Y. *Nano Today* **2015**, *10*, 355.
(7) Juarez-Perez, E. J.; Sanchez, R. S.; Badia, L.; Garcia-Belmonte, G.; Kang, Y. S.; Mora-Sero, I.; Bisquert, J. *J. Phys. Chem. Lett.* **2014**, *5*, 2390.
(8) Brenner, T. M.; Egger, D. A.; Kronik, L.; Hodes, G.; Cahen, D. *Nat. Rev. Mater.* **2016**, *1*, 15007.
(9) Stranks, S. D.; Eperon, G. E.; Grancini, G.; Menelaou, C.; Alcocer, M. J. P.; Leijtens, T.; Herz, L. M.; Petrozza, A.; Snaith, H. J. *Science* **2013**, *342*, 341.
(10) Szuromi, P. *Science* **2015**, *347*, 960.
(11) Oga, H.; Saeki, A.; Ogomi, Y.; Hayase, S.; Seki, S. *J. Am. Chem. Soc.* **2014**, *136*, 13818.
(12) Baumann, A.; Väth, S.; Rieder, P.; Heiber, M. C.; Tvingstedt, K.; Dyakonov, V. *J. Phys. Chem. Lett.* **2015**, *6*, 2350.
(13) Li, Y.; Meng, L.; Yang, Y.; Xu, G.; Hong, Z.; Chen, Q.; You, J.; Li, G.; Yang, Y.; Li, Y. *Nat. Commun.* **2016**, *7*, 10214.
(14) Susrutha, B.; Giribabu, L.; Singh, S. P. *Chem. Commun.* **2015**, *51*, 14696.
(15) Gu, Z.; Zuo, L.; Larsen-Olsen, T. T.; Ye, T.; Wu, G.; Krebs, F. C.; Chen, H. *J. Mater. Chem. A* **2015**, *3*, 24254.
(16) Schmidt, T. M.; Larsen-Olsen, T. T.; Carlé, J. E.; Angmo, D.; Krebs, F. C. *Adv. Energy Mater.* **2015**, *5*, 1500569.
(17) Hwang, K.; Jung, Y.-S.; Heo, Y.-J.; Scholes, F. H.; Watkins, S. E.; Subbiah, J.; Jones, D. J.; Kim, D.-Y.; Vak, D. *Adv. Mater.* **2015**, *27*, 1241.
(18) McGehee, M. D. *Nat. Mater.* **2014**, *13*, 845.
(19) Salim, T.; Sun, S.; Abe, Y.; Krishna, A.; Grimsdale, A. C.; Lam, Y. M. *J. Mater. Chem. A* **2015**, *3*, 8943.
(20) de Quilettes, D. W.; Vorpahl, S. M.; Stranks, S. D.; Nagaoka, H.; Eperon, G. E.; Ziffer, M. E.; Snaith, H. J.; Ginger, D. S. *Science* **2015**, *348*, 683.
(21) Eperon, G. E.; Burlakov, V. M.; Docampo, P.; Goriely, A.; Snaith, H. J. *Adv. Funct. Mater.* **2014**, *24*, 151.
(22) Park, N.-G. *CrystEngComm* **2016**, *18*, 5977.
(23) Bi, C.; Shao, Y.; Yuan, Y.; Xiao, Z.; Wang, C.; Gao, Y.; Huang, J. *J. Mater. Chem. A* **2014**, *2*, 18508.
(24) Aharon, S.; Layani, M.; Cohen, B.-E.; Shukrun, E.; Magdassi, S.; Etgar, L. *Adv. Mater. Interfaces* **2015**, *2*, 1500118.
(25) Yang, W. S.; Noh, J. H.; Jeon, N. J.; Kim, Y. C.; Ryu, S.; Seo, J.; Seok, S. I. *Science* **2015**, *348*, 1234.
(26) Burschka, J.; Pellet, N.; Moon, S.-J.; Humphry-Baker, R.; Gao, P.; Nazeeruddin, M. K.; Gratzel, M. *Nature* **2013**, *499*, 316.
(27) Wang, Q.; Shao, Y.; Dong, Q.; Xiao, Z.; Yuan, Y.; Huang, J. *Energy Environ. Sci.* **2014**, *7*, 2359.
(28) Liu, M.; Johnston, M. B.; Snaith, H. J. *Nature* **2013**, *501*, 395.
(29) Chen, Q.; Zhou, H.; Hong, Z.; Luo, S.; Duan, H.-S.; Wang, H.-H.; Liu, Y.; Li, G.; Yang, Y. *J. Am. Chem. Soc.* **2014**, *136*, 622.
(30) Bi, C.; Wang, Q.; Shao, Y.; Yuan, Y.; Xiao, Z.; Huang, J. *Nat. Commun.* **2015**, *6*, 8747.
(31) Wang, Q.; Dong, Q.; Li, T.; Gruverman, A.; Huang, J. *Adv. Mater.* **2016**, *28*, 6734.
(32) Yan, K.; Long, M.; Zhang, T.; Wei, Z.; Chen, H.; Yang, S.; Xu, J. *J. Am. Chem. Soc.* **2015**, *137*, 4460.
(33) Liang, P.-W.; Liao, C.-Y.; Chueh, C.-C.; Zuo, F.; Williams, S. T.; Xin, X.-K.; Lin, J.; Jen, A. K. Y. *Adv. Mater.* **2014**, *26*, 3748.
(34) Bi, D.; Tress, W.; Dar, M. I.; Gao, P.; Luo, J.; Renevier, C.; Schenk, K.; Abate, A.; Giordano, F.; Correa Baena, J.-P.; Decoppet, J.-D.; Zakeeruddin, S. M.; Nazeeruddin, M. K.; Grätzel, M.; Hagfeldt, A. *Sci. Adv.* **2016**, *2*, e1501170.
(35) Zuo, L.; Gu, Z.; Ye, T.; Fu, W.; Wu, G.; Li, H.; Chen, H. *J. Am. Chem. Soc.* **2015**, *137*, 2674.
(36) Jeon, N. J.; Noh, J. H.; Kim, Y. C.; Yang, W. S.; Ryu, S.; Seok, S. I. *Nat. Mater.* **2014**, *13*, 897.
(37) Kim, J.; Hwang, T.; Lee, S.; Lee, B.; Kim, J.; Jang, G. S.; Nam, S.; Park, B. *Sci. Rep.* **2016**, *6*, 25648.
(38) Rong, Y.; Venkatesan, S.; Guo, R.; Wang, Y.; Bao, J.; Li, W.; Fan, Z.; Yao, Y. *Nanoscale* **2016**, *8*, 12892−12899.
(39) Rong, Y.; Tang, Z.; Zhao, Y.; Zhong, X.; Venkatesan, S.; Graham, H.; Patton, M.; Jing, Y.; Guloy, A. M.; Yao, Y. *Nanoscale* **2015**, *7*, 10595.
(40) Ahn, N.; Son, D.-Y.; Jang, I.-H.; Kang, S. M.; Choi, M.; Park, N.-G. *J. Am. Chem. Soc.* **2015**, *137*, 8696.
(41) El-Henawey, M. I.; Gebhardt, R. S.; El-Tonsy, M. M.; Chaudhary, S. *J. Mater. Chem. A* **2016**, *4*, 1947.
(42) Liu, J.; Gao, C.; He, X.; Ye, Q.; Ouyang, L.; Zhuang, D.; Liao, C.; Mei, J.; Lau, W. *ACS Appl. Mater. Interfaces* **2015**, *7*, 24008.
(43) Li, Y.; Cooper, J. K.; Buonsanti, R.; Giannini, C.; Liu, Y.; Toma, F. M.; Sharp, I. D. *J. Phys. Chem. Lett.* **2015**, *6*, 493.
(44) Lian, J.; Wang, Q.; Yuan, Y.; Shao, Y.; Huang, J. *J. Mater. Chem. A* **2015**, *3*, 9146.
(45) Yu, H.; Liu, X.; Xia, Y.; Dong, Q.; Zhang, K.; Wang, Z.; Zhou, Y.; Song, B.; Li, Y. *J. Mater. Chem. A* **2016**, *4*, 321.
(46) Xiao, Z.; Dong, Q.; Bi, C.; Shao, Y.; Yuan, Y.; Huang, J. *Adv. Mater.* **2014**, *26*, 6503.
(47) Beckmann, P. A. *Cryst. Res. Technol.* **2010**, *45*, 455.
(48) Ke, W.; Fang, G.; Liu, Q.; Xiong, L.; Qin, P.; Tao, H.; Wang, J.; Lei, H.; Li, B.; Wan, J.; Yang, G.; Yan, Y. *J. Am. Chem. Soc.* **2015**, *137*, 6730.
(49) Kim, H.-S.; Lee, C.-R.; Im, J.-H.; Lee, K.-B.; Moehl, T.; Marchioro, A.; Moon, S.-J.; Humphry-Baker, R.; Yum, J.-H.; Moser, J. E.; Grätzel, M.; Park, N.-G. *Sci. Rep.* **2012**, *2*, 591.
(50) Chen, B.; Yang, M.; Priya, S.; Zhu, K. *J. Phys. Chem. Lett.* **2016**, *7*, 905.
(51) Noel, N. K.; Abate, A.; Stranks, S. D.; Parrott, E. S.; Burlakov, V. M.; Goriely, A.; Snaith, H. J. *ACS Nano* **2014**, *8*, 9815.
(52) Marco, N. D.; Zhou, H.; Chen, Q.; Sun, P.; Liu, Z.; Meng, L.; Yao, E.-P.; Liu, Y.; Schiffer, A.; Yang, Y. *Nano Lett.* **2016**, *16*, 1009.

DOI: 10.1021/jacs.6b09656
J. Am. Chem. Soc. 2016, 138, 15710−15716